Article

Quasi-Linearization Analysis for Entropy Generation in MHD Mixed-Convection Flow of Casson Nanofluid over Nonlinear Stretching Sheet with Arrhenius Activation Energy

Kashif Ali [1], Aftab Ahmed Faridi [2], Sohail Ahmad [3], Wasim Jamshed [4,*], Syed M. Hussain [5] and El Sayed M. Tag-Eldin [6]

1   Department of Basic Sciences and Humanities, Muhammad Nawaz Sharif University of Engineering and Technology, Multan 60000, Pakistan
2   Department of Mathematics, The Islamia University of Bahawalpur, Bahawalpur 63100, Pakistan
3   Centre for Advanced Studies in Pure and Applied Mathematics (CASPAM), Bahauddin Zakariya University, Multan 60800, Pakistan
4   Department of Mathematics, Capital University of Science and Technology (CUST), Islamabad 44000, Pakistan
5   Department of Mathematics, Faculty of Science, Islamic University of Madinah, Madinah 42351, Saudi Arabia
6   Electrical Engineering, Faculty of Engineering and Technology, Future University in Egypt, New Cairo 11835, Egypt
*   Correspondence: wasiktk@hotmail.com

Abstract: Thermal performance of magnetically driven Casson nanofluid over a nonlinear stretching sheet under the influence of entropy, activation energy and convective boundary conditions was analyzed numerically, employing the quasi-linearization method (QLM). The collective behavior of thermophoretic diffusion and Brownian motion along with special effects of viscous dissipation, thermal radiation, heat generation and joule heating are considered in the energy equation for the flow problem. The addition of nanoparticles helps to stabilize the flowing of a nanofluid and maintain the symmetry of the flowing structure. The governing highly nonlinear coupled differential equations of velocity, temperature, concentration and entropy are simulated through an iterative scheme encoded with MATLAB programming language. The geometric model is, therefore, described using a symmetry technique. A comparative analysis of linear and nonlinear stretching in sheets is presented via graphs and tables regarding pertinent dimensionless parameters. It is worth noting that the Nusselt number and Sherwood number decrease at relatively higher rates with growing values of activation energy in the case of nonlinear stretching. Moreover, the entropy generation rate near the stretching surface decreases due to the strong effects of Brownian motion and thermophoretic diffusion while it goes on improving far off the stretching surface.

Keywords: magnetohydrodynamics; Casson nanofluid; entropy generation; activation energy; quasi-linearization method

1. Introduction

The augmentation of heat transfer is essentially required in many thermal systems and it can be acquired by using nanofluids. The mixture of base fluid as well as nano-sized solid fragments gives rise to nanofluids (NFs) [1]. The pioneering concept of nanofluids was coined by Choi [2] before the end of the 20th century. Nano-sized suspended particles were supposed to enhance the heat transfer rate of fluids. Extending his concept, Choi [3] further presented a comprehensive review on fluid's nanotechnologies. Some pure metals, such as Copper, Iron, Platinum, Zinc and their oxides can act as nanomaterials and can be used in the preparation of nanofluids. The proficiency of conventional fluids can be boosted up using nanofluids that may effectively improve the thermal conductivity of common fluids [4–8]. The physical and thermal aspects of nanofluids have been much studied. Nanolaminates are a novel class of nanoparticles that illuminate the electrical,

chemical, physical and mechanical aspects of layer thickness during the fabrication of coating layers. Using molecular dynamics simulation, Doan [9] interpreted the indentation behavior of amorphous nanolaminates ($Cu_{80}Ta_{20}/Cu_{20}Ta_{80}$) under the simultaneous effects of surface interface and layer thickness. The impacts of surface layer, loading velocity and indenter size on nanolaminates mechanism were also justified in this study. Ekiciler et al. [10] examined the effect of different shapes of Al_2O_3 nanoparticles in the flow of water through a triangular duct with various volume fractions. Yadav et al. [11] conferred an inclusive review study on the nanoparticles of Carbon nanotubes (CNTs). They determined the physical and chemical stability of CNTs and claimed that Carbon nanotubes had better thermal properties and high tensile strength as compared to other nanomaterials. Arslan and Ekiciler [12] presented a numerical solution of the square duct flow problem of SiO_2/water nanofluid with 1.0% to 4.0% different volume fractions of nanoparticles. Ahmad et al. [13,14] numerically explored nanofluid flows under different circumstances using successive over-relaxation (SOR) technique.

The combination of non-Newtonian fluids (Casson, etc.) and nanoparticles has great potential in the field of bio-technology as well as in nanotechnologies related to life sciences. A time-independent type of Pseudo-plastic fluid, which possesses infinite and zero shear at zero and endless viscosity, respectively, can be referred to as Casson fluid. Some daily life fluids that can better describe the Casson fluids incorporate honey, soup, human blood, nail polish, jelly, liquid cement, tomato sauce, emulsions, etc. Casson [15] was the first who developed a model for this fluid and investigated the flow tendency of pigment oil. The proficient employments of nanofluids together with non-Newtonian fluids, such as Casson fluid, may be found in biomedical devices, biosensors, pharmaceuticals, agriculture, etc. Recently, Casson nanofluid flows have been explored under different effects. Shahzad et al. [16] deliberated the swirling Casson hybrid nanofluid flow taking the Darcy-Forchheimer formulation of the porous medium. The flow was taken through parallel plates. It was noted that how much the thermal characteristics changed with porosity, viscous fluid nature, rotational coordinates and magnetic interactions. The heat transfer flow of Casson hybrid nanofluids comprising Silver and Titania nanoparticles was explained by Krishna et al. [17]. In this analysis, base Casson fluid involved water and ethylene glycol. The concentration and thermal buoyancy forces increased the flow velocity. Casson fluid was treated as blood flowing through a narrow artery [18]. Skin friction and flow velocity were determined using Newtonian fluid (stenosis artery case) and non-Newtonian fluid (normal artery).

Use of entropy generation to control the irreversibility in the thermal systems is essentially required. Obalalu [19] developed a mathematical model to analyze the non-Darcian and non-Newtonian Casson nanofluid boundary layer flow in the environment of slip condition and entropy generation. Chebyshev collocation method was used to acquire the iterative solutions. The change in thermophysical properties due to the involvement of internal energy in the Casson flow was examined by Salahuddin et al. [20]. Diffusivity, conductivity and viscosity were assumed to be temperature dependent. An increase in temperature was noticed in response to employing the activation energy to the flow regime. Hirpho et al. [21] considered the mixed convective flow within an enclosure having wavy walls. The Casson fluid was kept at the heated bottom wavy wall, whereas two walls of the enclosure were assumed to be at cold temperature. They determined that an increase in Nusselt number occurred because of an increase in Richardson number. Ennaouri & Hachem [22] carried out an analysis of arterial Casson nanofluid blood flow, in which effects of various parameters on blood flow were noticed. Blood-based Casson nanofluid flow was numerically examined by Jamil et al. [23]. Further novel investigations of Casson nanofluids subject to different effects can be searched from refs. [24–26].

The pertinence of flows over nonlinear/linear extending sheet is found in some industrial processes, such as polymer sheet dying process, metallic plate condensation process and plastic sheets extrusion process. Choosing the stretching rate for the sheet is important as it can influence the final quality of the desired products. A Darcy-Forchheimer flow of

nanoparticles and Casson flow compelled by a nonlinear and unsteady stretching surface was analyzed, respectively, by Rasool et al. [27] and Oyelakin et al. [28]. An analysis of Eyring–Powell nanofluid, which depicted the importance of thermal conductivity and dynamic viscosity for a stretching sheet, was presented by Lawal et al. [29]. Flow formation parameters were discussed against temperature, surface drag and concentration. Vishalakshi et al. [30] studied the Graphene-nanoparticle-based flow with allowance for thermal radiation involving mass transpiration and slip conditions. The porous stretching/shrinking sheet was taken as geometry in this analysis. It was deduced that the viscoelastic parameter would cause an increase in the temperature. Seid et al. [31] mathematically treated a dynamical heat transfer problem through a vertical stretching sheet assuming the special effects of the Soret and Dufour fluxes. Moreover, the analytic results were compared with those obtained from the optimal homotopy analysis method.

The magnetic nanoparticles have great significance in the adjustable fiber filters, treatment of cancer in medicine, modulators and optical controls. As time has gone on, many scientists and research scholars have investigated Casson nanofluid flows under the influence of externally designed magnetic field settings. Alali and Megahed [32] examined the dissipation phenomenon and the effects of slip velocity on the magnetohydrodynamic non-Newtonian Casson thin-film flow. They simplified governing equations using similarity variables and, consequently, obtained a dimensionless system with eight dominant parameters. Sadiq et al. [33] observed the rate of mass and heat transport in the Casson nanofluid flow inside a confined channel under the incitement of ramped temperature, magnetic field and ramped concentration. The Sodium alginate was used as a base fluid in the preparation of nanofluid. It was concluded that ramped conditions would better control the flow and thermal properties of the nanofluid. The Darcy-Forchheimer effects were considered by Jawad et al. [34] in MHD flow of Casson nanofluid. The Arrhenius stimulation energy effect was also taken into account by the authors in the flow model. In this research, the homotopy analysis method was preferably used to determine the numerical solutions. A hydromagnetic flow induced by the nonlinear extending sheet and involving Casson nanofluids was investigated by Ullah et al. [35]. They developed tabular data for wall shear stress and presented a comparison of their results with the existing literature. The outcomes depicted that Casson nanofluid caused a control on temperature in the presence of a magnetic field. Al-Kouz and Owhaib [36] and Bejawada et al. [37] presented numerical studies of Casson nanofluid flows over linear and nonlinear surfaces under MHD effects, respectively. The results of both papers revealed that the impact of Casson fluid factor was to reduce the velocities in fluids. Analytical as well as numerical techniques were employed by researchers in the modern era to resolve the coupled nonlinear systems encountered in the fluid flow problems with nanocomposites. Bala Anki Reddy et al. [38] presented quite unique technique of an artificial neural network (ANN) to solve the MHD cross nanofluid flow problem, taking into account the thermophoresis and Brownian motion effects simultaneously. Praveen et al. [39] employed the finite volume method to simulate the governing equations of flow in water-based fly ash nanofluid. The authors further extended the study [40–42] by experimental and computational analysis of heat transfer, pressure drop, entropy generation and friction factor, through a horizontal copper tube. In more recent times, Ali et al. [43] engaged the finite element method to observe thermal radiation effects in the presence of a magnetic field, considering the motile microbe gyration in the water-based nanofluid. The authors of [44–51] presented the latest update involving traditional nanofluids with the features of heat and mass transmission in a different physical situation.

The available literature reveals the fact that the flow of Casson nanofluid over a nonlinear stretching sheet has not been explored yet, taking the simultaneous impacts of entropy and activation energy under the magnetohydrodynamic environment, employing a persuasive numerical approach; the quasi-linearization method (QLM). To establish a mathematical model that describes the activation energy and entropy generation phenomenon in MHD mixed-convective Casson nanofluid flow over a nonlinear stretching sheet is the

main focus of this work. The preeminent parameters are interpreted via the graphical and tabular representations. In order to determine the iterative solution, an algorithm based on linearization of coupled and nonlinear equations is developed. This technique provides an easy approach towards finding the solution of complex dynamical problems. The role of magnetic interaction, mixed convection, thermophoretic diffusion, Brownian motion and Arrhenius activation energy was discussed for Casson nanofluids.

2. Formulation of Flow Model

Let us assume a steady, two-dimensional, mixed-convection hydro magnetic flow of conducting Casson nanofluid generated due to nonlinear stretching sheet structured by chemical reaction, slip and convective boundary conditions. The velocity of the wall of the stretching sheet is supposed $u_w(x) = ax^m$, where a is constant and m is index parameter. The sheet is oriented in the direction of the x-axis while the stream of flow is taken along the y-axis, as projected in Figure 1. A magnetic field of strength B_0 is controlling all boundary layers along with the joule heating phenomenon. Ambient conditions for thermal and solutal streams are T_∞ and C_∞, respectively.

$$u = u_w + N_1\left(1 + \frac{1}{\beta}\right)\mu_f\frac{\partial u}{\partial y}, \; v = V_w, \; k_f\frac{\partial T}{\partial y} = -h_f\left(T_f - T\right), \; k_s\frac{\partial C}{\partial y} = -h_s\left(C_w - C\right)$$
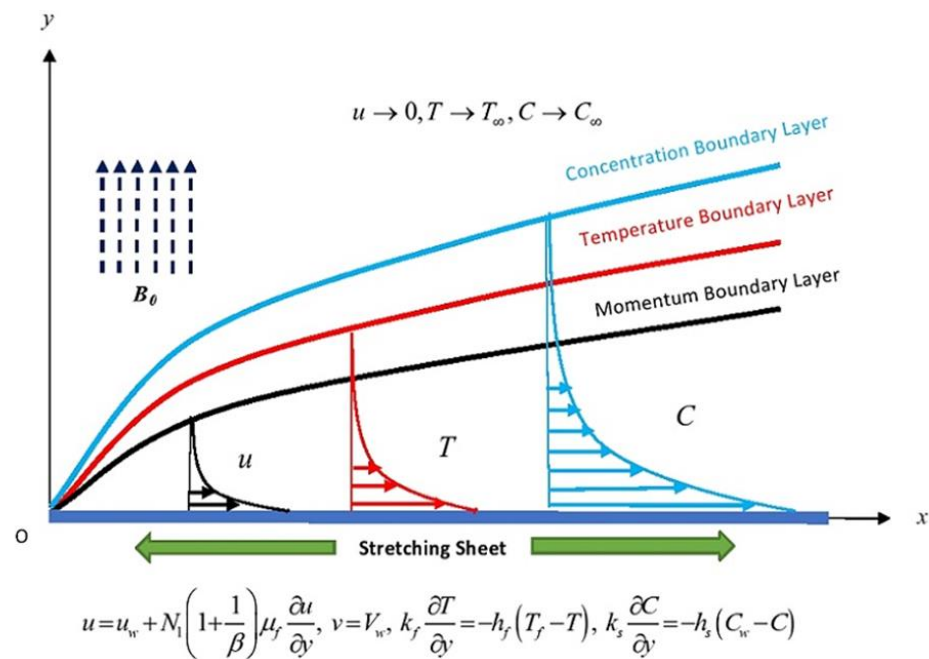
Figure 1. Flow configuration.

The basic rheological relations for mass, momentum, energy and concentration are given as [52,53]:

$$\frac{\partial u}{\partial x} + \frac{\partial v}{\partial y} = 0 \tag{1}$$

$$u\frac{\partial u}{\partial x} + v\frac{\partial u}{\partial y} = \frac{\mu_f}{\rho_f}\left(1 + \frac{1}{\beta}\right)\frac{\partial^2 u}{\partial y^2} - \frac{\sigma B_0^2(x)}{\rho_f}u$$
$$+ \left[(1 - C_\infty)\frac{\rho_{f\infty}}{\rho_f}\beta_T(T - T_\infty) - \frac{(\rho_p - \rho_{f\infty})}{\rho_f}(C - C_\infty)\right]g \tag{2}$$

$$u\frac{\partial T}{\partial x} + v\frac{\partial T}{\partial y} = \alpha_f\frac{\partial^2 T}{\partial y^2} + \tau\left[D_B\frac{\partial C}{\partial y}\frac{\partial T}{\partial y} + \frac{D_T}{T_\infty}\left(\frac{\partial T}{\partial y}\right)^2\right]$$
$$- \frac{1}{(\rho c)_f}\frac{\partial q_r}{\partial y} + \frac{\mu_f}{(\rho c)_f}\left(1 + \frac{1}{\beta}\right)\left(\frac{\partial u}{\partial y}\right)^2 + \frac{\sigma B_0^2}{(\rho c)_f}u^2 + \frac{Q}{(\rho c)_f}(T - T_\infty) \tag{3}$$

$$u\frac{\partial C}{\partial x} + v\frac{\partial C}{\partial y} = D_B\frac{\partial^2 C}{\partial y^2} + \frac{D_T}{T_\infty}\frac{\partial^2 T}{\partial y^2} - k_r^2(C - C_\infty)\left(\frac{T}{T_\infty}\right)^n e^{\left(-\frac{E_a}{kT}\right)} \tag{4}$$

The above-cited mathematical relations are composed of u and v being the velocity components in the x and y directions, respectively. Moreover, the symbols used for description of modelled equations and are: β; Casson material parameter, μ_f; dynamic viscosity of fluid, σ; electrically conductivity, ρ_f; fluid density, g; gravitational force due to acceleration, β_T; volumetric coefficient of thermal expansion, D_B; Brownian diffusion coefficient, D_T; thermophoretic diffusion coefficient, $\alpha_f \left(= k/(\rho c)_f \right)$; thermal diffusivity of the fluid, $\tau \left(= (\rho c)_p/(\rho c)_f \right)$; ratio of heat capacities of fluid and nanoparticles, q_r; radiative heat flux, k_r^2; rate of chemical reaction and E_a; activation energy factor.

Boundary conditions of the sheet are given as:

$$\left. \begin{array}{l} u = u_w + N_1 \left(1 + \frac{1}{\beta}\right) \mu_f \frac{\partial u}{\partial y}, v = V_w, k_f \frac{\partial T}{\partial y} = -h_f \left(T_f - T\right), k_s \frac{\partial C}{\partial y} = -h_s (C_w - C) \text{ at } y = 0, \\ \\ u \to 0, \ T \to T_\infty, \ C \to C_\infty \text{ as } y \to \infty. \end{array} \right\} \quad (5)$$

In Equation (5), the symbols used, N_1; the slip factor, h_f; heat convection and h_s; mass flow are expressed by the following relations $N_1 = N_0 x^{-\left(\frac{m-1}{2}\right)}$, $h_f = h_0 x^{\left(\frac{m-1}{2}\right)}$, and $h_s = h_0 x^{\left(\frac{m-1}{2}\right)}$.

The well-known Rosseland approximation is employed to describe the radiative heat flux q_r in the energy equation

$$q_r = \frac{-4\sigma^*}{3k_1{}^*} \frac{\partial T^4}{\partial y} \quad (6)$$

where σ^* is the Stefan–Boltzmann constant and $k_1{}^*$ is the mean absorption coefficient. To evaluate T^4 as a linear function of temperature, we expand T^4 by Taylor' series approximation about T_∞. Truncating higher-order terms, we obtain

$$T^4 \cong 4T_\infty^3 T - 3T_\infty^4 \quad (7)$$

Here, we define a new set of similarity variables corresponding to the stream function (ψ), temperature (T) and concentration (C) comprising a similar variable ξ,

$$\xi = \sqrt{\frac{(m+1)ax^m}{2\nu x}}y, \ \psi = \sqrt{\frac{2\nu ax^{m+1}}{m+1}}f(\xi), \ \theta(\xi) = \frac{T - T_\infty}{T_f - T_\infty}, \ \phi(\xi) = \frac{C - C_\infty}{C_w - C_\infty} \quad (8)$$

The new variables defined in Equation (8) yield the transformed system of Equations (9)–(12) on plugging into the modelled Equations (2)–(5).

$$\left(1 + \frac{1}{\beta}\right)f''' + ff'' - \frac{2m}{m+1}f'^2 - \frac{2}{m+1}Mf' + \lambda(\theta + N\phi) = 0 \quad (9)$$

$$\frac{1}{\mathrm{Pr}}\left(1 + \frac{4}{3}R_d\right)\theta'' + f\theta' + N_b\phi'\theta' + N_t\theta'^2 + \left(1 + \frac{1}{\beta}\right)Ecf''^2 + MEcf'^2 + \varepsilon\theta = 0 \quad (10)$$

$$\frac{1}{Le}\phi'' + f\phi' + \frac{N_t}{N_b}\theta'' - \left(\frac{2}{m+1}\right)k_1(1 + \alpha_1\theta)^n \phi \exp\left(\frac{-E}{1 + \alpha_1\theta}\right) = 0 \quad (11)$$

The associated boundary conditions are given as

$$\left. \begin{array}{l} f'(0) = 1 + \sqrt{\frac{m+1}{2}}\delta\left(1 + \frac{1}{\beta}\right)f''(0), \ \theta'(0) = -\sqrt{\frac{2}{m+1}}Bi_1[1 - \theta(0)], \\ \\ \phi'(0) = -\sqrt{\frac{2}{m+1}}Bi_2[1 - \phi(0)], \text{ and } f'(\infty) = 0, \ \theta(\infty) = 1, \ \phi(\infty) = 0 \end{array} \right\} \quad (12)$$

In the above expressions, the dimensionless parameters M, λ, N, Pr, R_d, N_t, N_b, Ec, ε, Le, k_1, α_1, E, δ, Bi_1, Bi_2 and Gr are the magnetic parameter, mixed convection, buoyancy forces ratio, Prandtl number, radiation parameter, thermophoresis parame-

ter, Brownian motion parameter, Eckert number, heat generation ($\varepsilon > 0$) or absorption ($\varepsilon < 0$) parameter, Lewis number, reaction rate, temperature gradient, activation energy parameter, slip parameter, thermal Biot number, solutal Biot number and Grashof number, respectively, and are defined by the following relations as: $M = \frac{2\sigma B_0^2}{a\rho_f(m+1)}$, $\lambda = \frac{Gr}{Re_x^2}$, $N = \frac{(\rho_p - \rho_{f\infty})(C_w - C_\infty)}{(1 - C_\infty)\rho_{f\infty}\beta_T(T_f - T_\infty)}$, $Pr = \frac{\nu_f}{\alpha_f}$, $R_d = \frac{4\sigma^* T_\infty^3}{kk_1^*}$, $N_t = \frac{\tau D_T(T_f - T_\infty)}{\nu}$, $N_b = \frac{\tau D_B(C_w - C_\infty)}{\nu}$, $Ec = \frac{u_w^2}{c_f(T_f - T_\infty)}$, $\varepsilon = \frac{2xQ}{(\rho c)_f(m+1)u_w}$, $Le = \frac{\nu}{D_B}$, $k_1 = \frac{k_r^2}{a}$, $\alpha_1 = \frac{T_f - T_\infty}{T_\infty}$, $E = \frac{-E_a}{kT_f}$, $\delta = N_1\sqrt{\frac{a}{\nu}}$, $Bi_1 = \frac{h_f}{k_f}\sqrt{\frac{\nu}{a}}$, $Bi_2 = \frac{h_s}{k_s}\sqrt{\frac{\nu}{a}}$ and $Gr = \frac{(1 - C_\infty)(\rho_{f\infty}/\rho_f)g\beta_T(T_\infty - T_m)x^3}{\nu^2}$.

The wall skin friction, wall heat flux and wall mass flux, respectively, are defined by

$$\tau_w = \mu\left(1 + \frac{1}{\beta}\right)\left(\frac{\partial u}{\partial y}\right)^2_{y=0}, \; q_w = -\left(\left(\alpha_f + \frac{16\sigma^* T_\infty^3}{3\rho c_p k_1^*}\right)\frac{\partial T}{\partial y}\right)_{y=0}, q_s = -D_B\left(\frac{\partial C}{\partial y}\right)_{y=0}$$

The skin friction coefficient $Cf_x = \frac{2\tau_w}{\rho_f u_w^2}$, the local Nusselt number $Nu_x = \frac{xq_w}{\alpha_f(T_f - T_\infty)}$ and local Sherwood number $Sh_x = \frac{xq_s}{D_B(C_w - C_\infty)}$ on the surface along x-direction are the dimensionless physical quantities. Where the local Nusselt number Nu_x and Sherwood number Sh_x are given by

$$\left.\begin{array}{l}(Re_x)^{1/2}Cf_x = \left(\frac{m+1}{2}\right)\left(1 + \frac{1}{\beta}\right)f''(0), \quad (Re_x)^{-1/2}Nu_x = -\left(\frac{m+1}{2}\right)\left(1 + \frac{4}{3}R_d\right)\theta'(0), \\ (Re_x)^{-1/2}Sh_x = -\left(\frac{m+1}{2}\right)\phi'(0)\end{array}\right\} \tag{13}$$

where $Re_x = \frac{ax^{m-1}}{\nu}$ is the local Reynold number.

3. Entropy Generation Analysis

A mathematical expression for entropy generation due to heat, fluid friction, magnetic retardation and mass concentration is written as

$$S_G = \frac{k}{T_\infty^2}(1 + \frac{16\sigma^* T_\infty^3}{3kk^*})\left(\frac{\partial T}{\partial y}\right)^2 + \frac{\sigma B^2(x)}{T_\infty}u^2 + \frac{1}{T_\infty}\left(1 + \frac{1}{\beta}\right)\left(\frac{\partial u}{\partial y}\right)^2 + \frac{RD_B}{T_\infty}\frac{\partial C}{\partial y}\frac{\partial T}{\partial y} + \frac{RD_B}{C_\infty}\left(\frac{\partial C}{\partial y}\right)^2 \tag{14}$$

Which after simplification gives the form

$$\begin{aligned}N_G &= \left(1 + \frac{4}{3}R_d\right)\left(\frac{m+1}{2}\right)\theta'^2\alpha_1 + MBrf'^2 \\ &\quad + \left(\frac{m+1}{2}\right)\left(1 + \frac{1}{\beta}\right)B_rf'^2 + \left(\frac{m+1}{2}\right)\chi\lambda_1\phi'\theta' + \left(\frac{m+1}{2}\right)\frac{L}{\alpha_1}\phi'^2\end{aligned} \tag{15}$$

Here

$$N_G = \frac{\nu S_G T_\infty}{ak\left(T_f - T_\infty\right)}x^{1-m}, \; Br = \frac{\mu a^2 x^{2m}}{k\left(T_f - T_\infty\right)}, \; \chi = \frac{(C_w - C_\infty)}{C_\infty}, \; \lambda_1 = \frac{RD_B(C_w - C_\infty)}{k}$$

where N_G, Br, χ and λ_1 are the rate of entropy optimization, Brinkman number, concentration gradient and diffusive variable, respectively.

4. Solution Procedure

The solution of the modelled equations for MHD Casson nanofluid flow over a nonlinear stretching sheet may be found numerically by solving the linear system of equations, obtained from the set of coupled nonlinear differential equations, by employing a persuasive technique, known as the quasi-linearization method (QLM). A sequence of auxiliary vectors $\left\{f^{(k)}\right\}$, $\left\{\theta^{(k)}\right\}$ and $\left\{\phi^{(k)}\right\}$ is generated through this method, corresponding to the "k^{th}"

linearized equations related to foremost functions f, θ and ϕ, such that Equations (9)–(11) can be rewritten as:

$$\left(1 + \tfrac{1}{\beta}\right)f^{(k+1)'''} + f^{(k)}f^{(k+1)''} - \tfrac{4m}{m+1}f^{(k)'}f^{(k)''}f^{(k+1)'} - \tfrac{2}{m+1}Mf^{(k+1)'}$$
$$= f^{(k)}f^{(k)''} - \tfrac{2m}{m+1}f^{(k)'2} - \tfrac{4m}{m+1}f^{(k)'2}f^{(k)''} - \lambda(\theta + N\phi) \tag{16}$$

$$\tfrac{1}{Pr}\left(1 + \tfrac{4}{3}R_d\right)\theta^{(k+1)''} + f^{(k)}\theta^{(k+1)'} + N_b\phi^{(k)'}\theta^{(k+1)'} + N_t\theta^{(k+1)'2}$$
$$+ (1 + \tfrac{1}{\beta})Ecf^{(k)''^2} + MEcf^{(k)'2} + \varepsilon\theta^{(k+1)} = 0 \tag{17}$$

$$\tfrac{1}{Le}\phi^{(k+1)''} + f^{(k)}\phi^{(k+1)'} + \tfrac{N_t}{N_b}\theta^{(k)''} - \left(\tfrac{2}{m+1}\right)k_1(1 + \alpha_1\theta^{(k)})^n \phi \exp(\tfrac{-E}{1 + \alpha_1\theta^{(k)}}) = 0 \tag{18}$$

The simulation of a linearized system in Equations (16)–(18) is iteratively proceeded through MATLAB programming and a stopping criterion for the maximum difference between the numerical solutions of two consecutive iterates is defined by the following inequalities:

$$\max\left(\left\|f^{(k+1)} - f^{(k)}\right\|_{L_2}, \left\|\theta^{(k+1)} - \theta^{(k)}\right\|_{L_2}, \left\|\phi^{(k+1)} - \phi^{(k)}\right\|_{L_2}\right) < 10^{-8} \tag{19}$$

Additional information related to this iterative procedure may be found in our anterior literature [54–57]. Figure 2 summarizes the order of numerical procedure adopted in simulation of the problem. A graphical comparison presented in Figure 3 validates our numerical procedure with the classical results by Vajravelu [58].
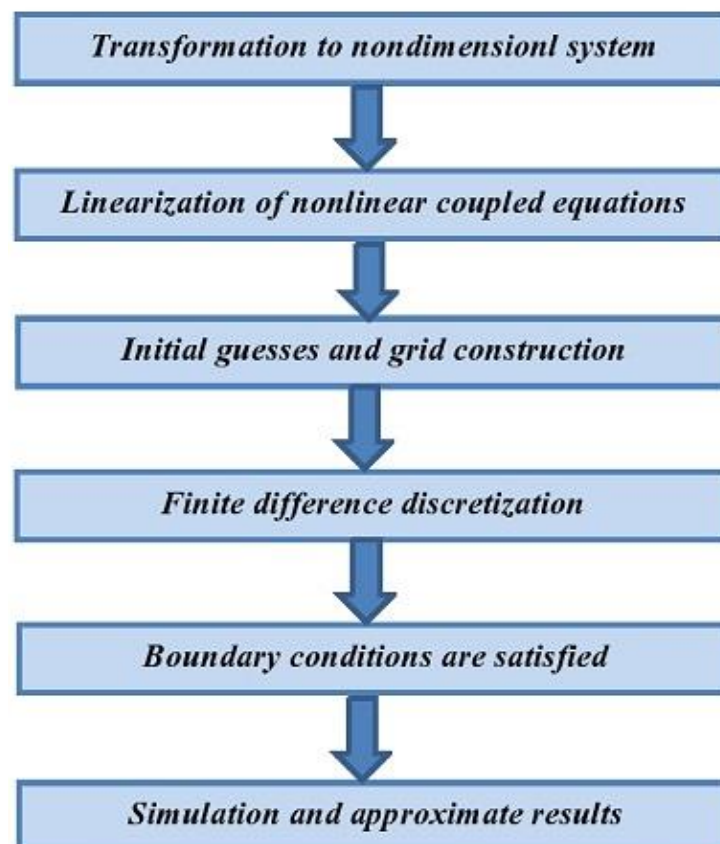

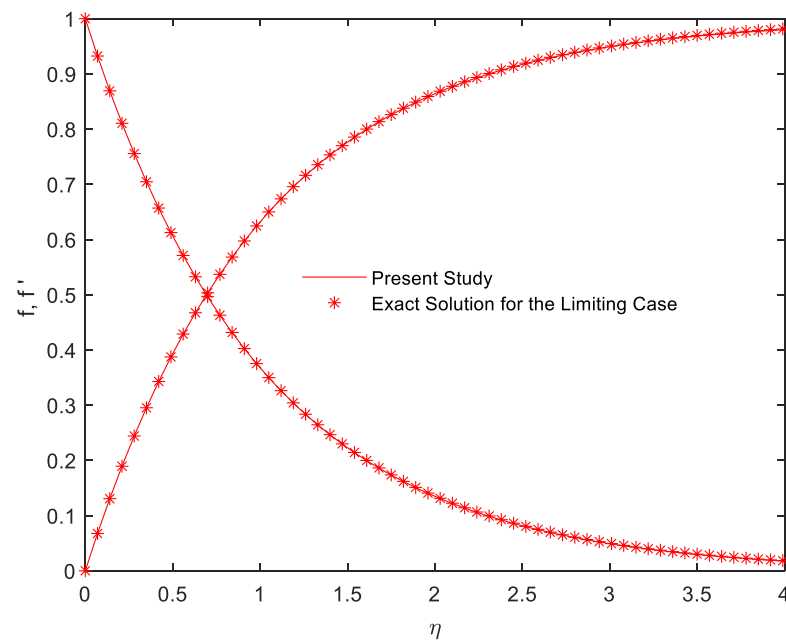**Figure 2.** Flow diagram of simulation methodology.

Figure 3. Comparison of numerical scheme adopted in the present study over nonlinear stretching sheet with the classical analytical results.

5. Results and Discussion

The flow and mass transfer analysis of magnetically driven Casson nanofluid over a nonlinear stretching sheet is performed numerically for two distinctive index numbers $m = 1.0$ and $m = 10$ in a single frame. The governing nonlinear differential equations of the flow regime are numerically simulated through the quasi-linearization method (QLM) for all three types of boundary layers (i.e., velocity, temperature and concentration boundary layers). The major parameters that are controlling the flow system are estimated through graphical as well as tabular data for the following set of default values fixed as: $Bi_1 = 3$, $Bi_2 = 2$, $M = 10$, $\beta = 0.3$, $S = 1.0$, $\Pr = 7.38$, $N_b = 0.2$, $N_t = 0.1$, $\varepsilon = 0.5$, $Ec = 0.1$, $Le = 1.0$, $Rd = 1.0$, $N = 0.5$, $\lambda = 5.0$, $E = 5.0$, $k_1 = 0.5$, $\alpha_1 = 2.0$, $\delta = 0.5$, $\lambda_1 = 0.2$, $n_0 = 0.5$, $L = 1.0$, $Br = 0.5$ and $\chi = 0.5$.

5.1. Velocity Profiles

Figures 4–7 show the influence of various parameters on the velocity profiles of MHD Casson nanofluid flow for two distinct indices m ($m = 1.0$ and $m = 10$). Figure 4 displays that the velocity curves decline for increasing values of the magnetic parameter for both linear and nonlinear stretching cases, but the impact of linear stretching is more prominent as compared to the nonlinear one. Physically, magnetic field produces a resistive force in the flow region that retards the fluid acceleration. A similar trend can be observed in Figure 5 for the Casson parameter. The reason behind this decline in velocity is due the expanding plastic viscosity in the Casson fluid. Here, the nonlinear stretching dominates the linear stretching significantly. Figure 6 shows that the influence of slip parameter is to fall off the fluid's acceleration due to the wall shear stress factor. The decline in velocity distribution for linear stretching is higher than that of nonlinear stretching. The impact of increasing values of buoyancy force ratio on the velocity profiles is to accelerate the fluid extraordinarily (see Figure 7). Physically, the buoyant forces enhance the thickness of the momentum boundary layer and, hence, the fluid's velocity as well.
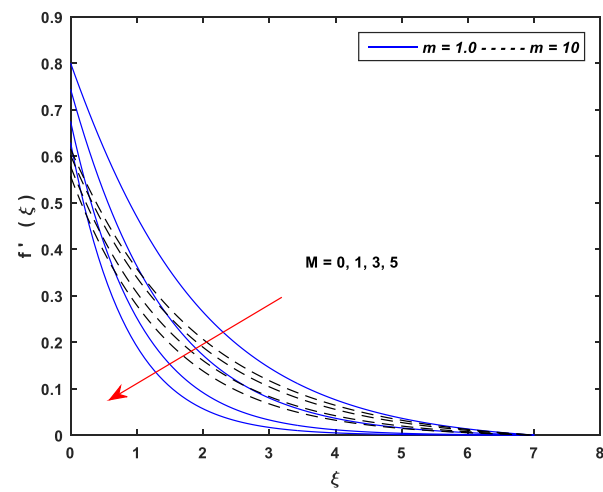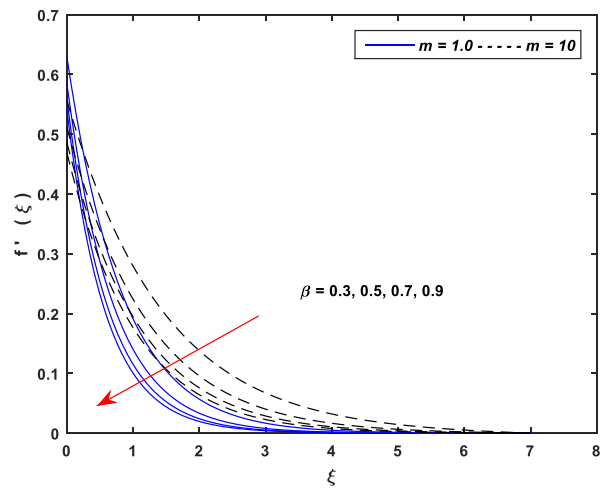
Figure 4. Delineation of $f'(\xi)$ for various M.

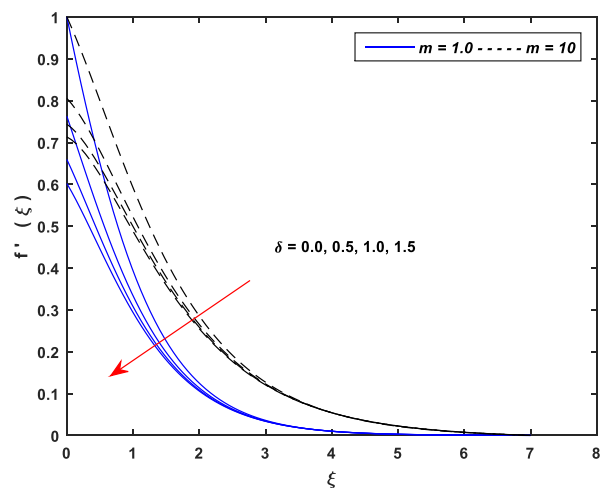

Figure 5. Delineation of $f'(\xi)$ for various β.

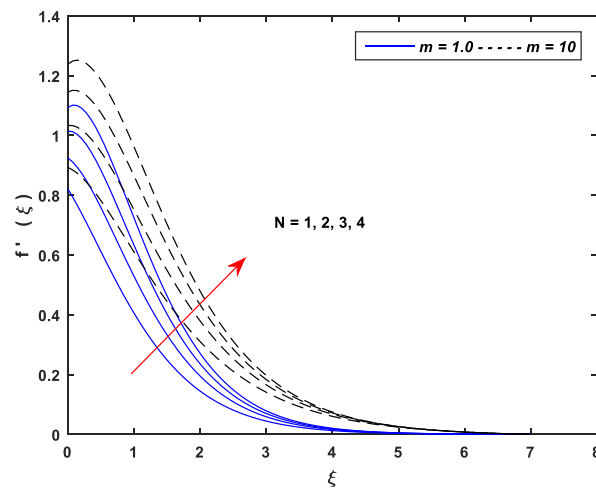**Figure 6.** Delineation of $f'(\xi)$ for various δ.

Figure 7. Delineation of $f'(\xi)$ for various N.

5.2. Thermal Profiles

Figures 8–17 exhibit the impact of various parameters on the temperature curves of the flow. Figure 8 states that the increasing values of magnetic parameter upsurge the thermal profiles for both linear and nonlinear stretching cases. Drag force generated due to the magnetic field produces the friction to flow, which incidentally enhances the heat of flowing fluid. Impact of the Casson parameter shows quite opposite behavior as compared to the magnetic parameter. The rising Casson parameter reduces the yield stress, which, in turn, depletes the thermal boundary layer thickness and, hence, shows a significant decline in thermal profiles (see Figure 9). Figures 10 and 11 describe that the increment in mixed convection parameter and Eckert number lead to rapid rise in thermal profiles due to nonlinear stretching in contrast with the linear stretching case. The abrupt upsurge in heat of fluid is due to the dissipative heat generated due to frictional aspects of adjacent layers.
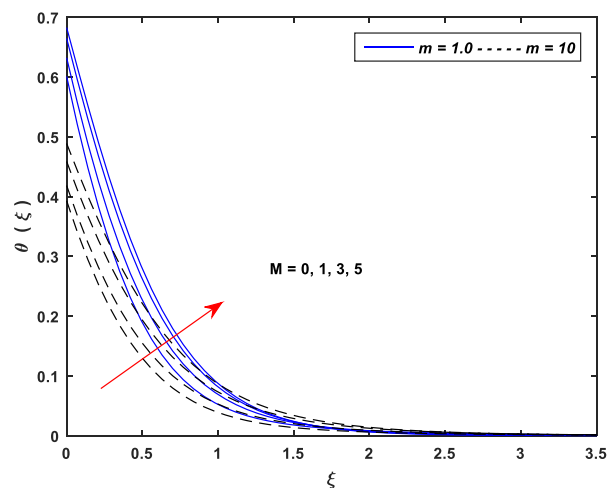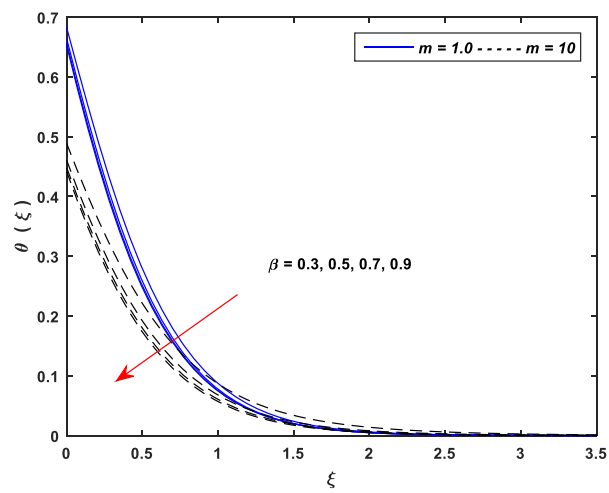

Figure 8. Delineation of $\theta(\xi)$ for various M.
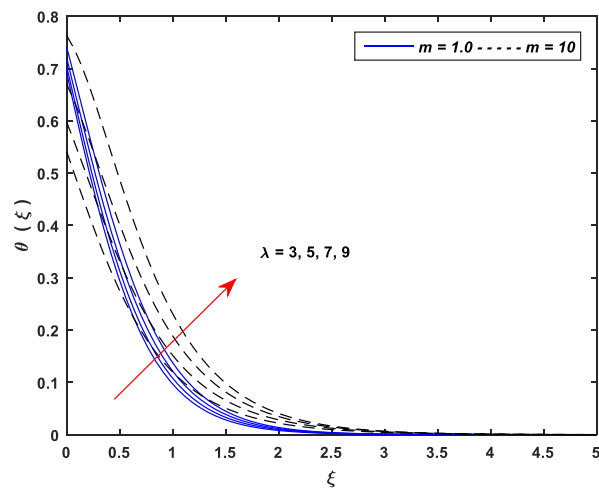
Figure 9. Delineation of $\theta(\xi)$ for various β.

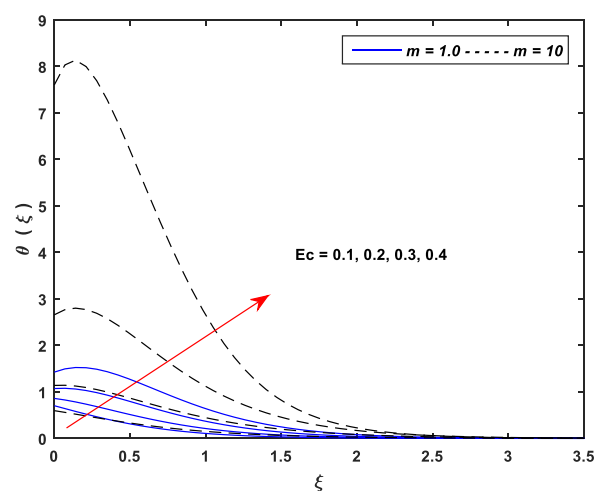**Figure 10.** Delineation of $\theta(\xi)$ for various λ.

Figure 11. Delineation of $\theta(\xi)$ for various Ec.
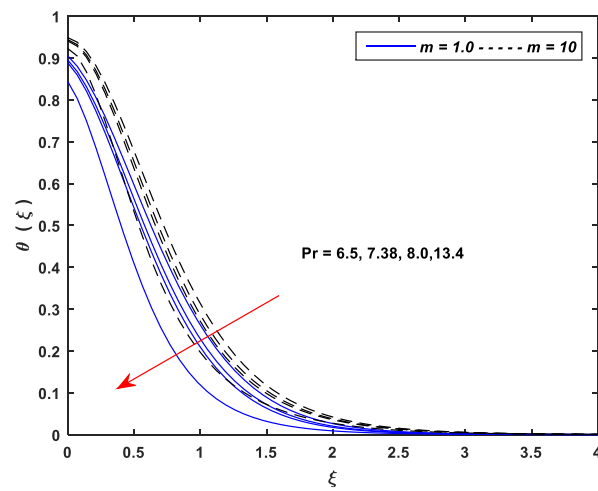
Figure 12. Delineation of $\theta(\xi)$ for various Pr.

Figure 13. Delineation of $\theta(\xi)$ for various *Rd*.

Figure 14. Delineation of $\theta(\xi)$ for various ε.
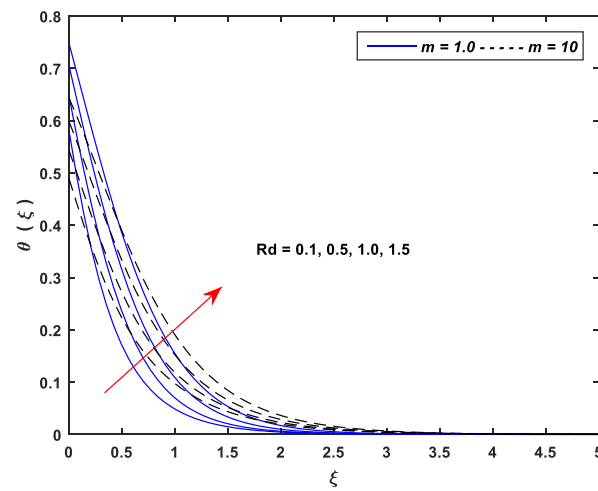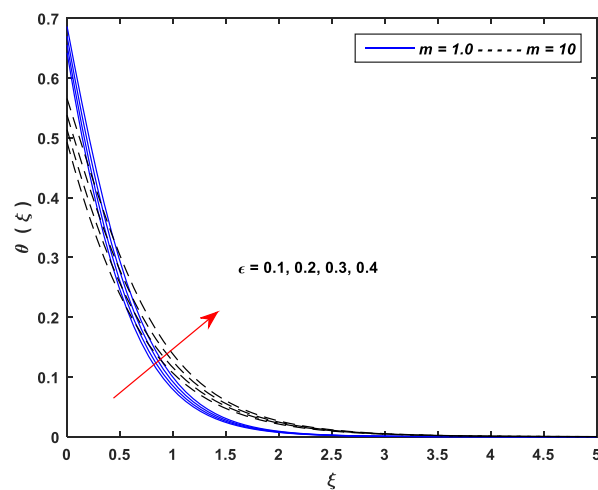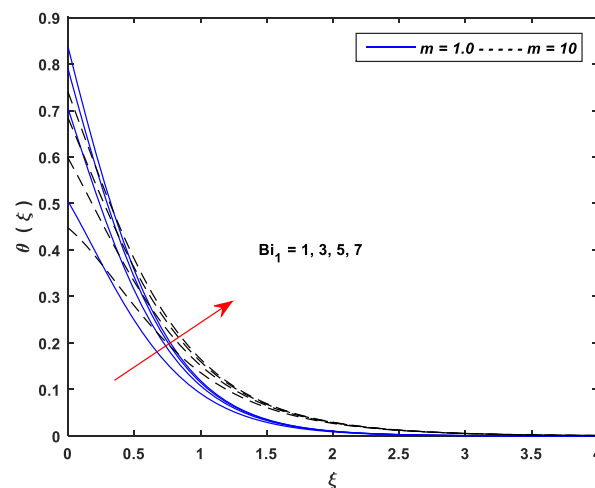
Figure 15. Delineation of $\theta(\xi)$ for various Bi_1.
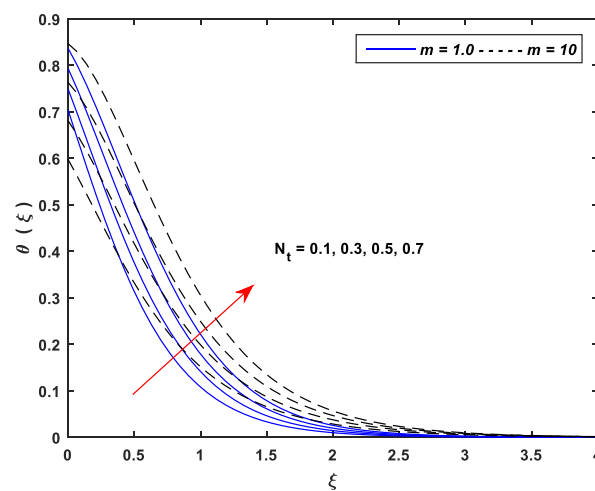
Figure 16. Delineation of $\theta(\xi)$ for various N_t.
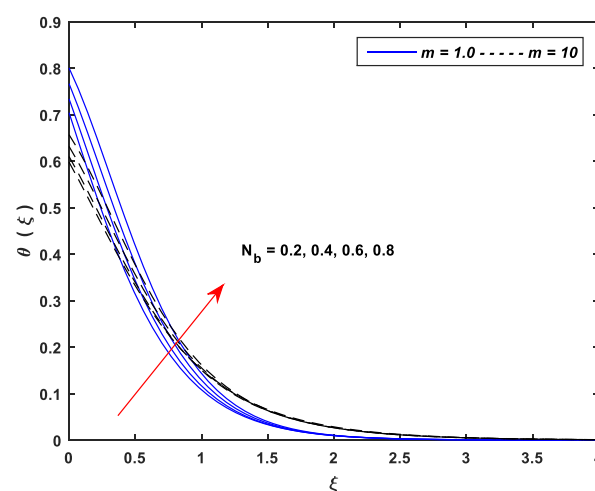
Figure 17. Delineation of $\theta(\xi)$ for various N_b.

Figure 12 demonstrates that by enlarging the Prandtl number, dwindling effects on the thermal profiles are observed. The range of Prandtl number has been chosen for different working non-Newtonian fluids (i.e., Sodium alginate, methanol, and sea-water etc.). Figure 13 reveals that the thermal radiation effects increase the heat transfer rate of the fluid, subsiding the heat absorption rate. The heat generation parameter enhances the

thermal distribution for both indices m ($m = 1.0$ and $m = 10$). Nonlinear stretching shows a higher upsurge in thermal distributions for $1 \leq \xi \leq 3$ (see Figure 14). Thermal Biot number Bi_1 given in Figure 15 shows an increasing effect on the thermal profiles. Physically, thermal Biot number enhances the convection of heat by reducing the surface retardation effects. Hence, the thermal boundary layer thickness improves and the temperature of the fluid rises accordingly. Figures 16 and 17 are sketched to show the impact of thermophoresis and Brownian motion on the thermal curves. Thermophoresis depends on the thermal gradient, which tends to enhance the heat of fluid on increasing the values of N_t for both cases of stretching. However, nonlinear stretching dominates the linear one for relatively higher values of the domain. A similar trend was seen for the Brownian motion parameter N_b. Physically, the random motion of nanoparticles increases the kinetic energy of flow due to collisions of nanoparticles, which ultimately transform into heat energy. Hence, the overall heat of the flow region enhances and raises the thermal profiles.

5.3. Concentration Profiles

Figures 18–25 are prepared to discuss the effects of principal parameters on the solutal profiles. It is evident from graphical data that the linear stretching leads the nonlinear stretching for all governing parameters of the concentration profiles. Figure 18 shows that the mixed convection parameter improves the concentration profiles with its rising values while buoyancy force ratio has fairly opposite behavior on the solutal profiles (see Figure 19). All these physical impacts are due to a combination of Ohmic heating and Lorentz force produced at the surface of a nonlinear stretching sheet. Figures 20 and 21 are prepared to show the effects of thermophoresis and Brownian motion on the solutal profiles. Increasing values of N_t, enhance the concentration of nanoparticles. Physically, enlarging the thermophoretic parameter, the temperature difference rises, which improves the thermophoresis diffusion. Hence, the concentration of governing fluid raises in the flow regime. On the contrary, augmenting the Brownian motion parameter N_b, concentration profiles diminish significantly. Random motion of nanoparticles heats up the fluid and accelerates the heated nanoparticles away from the stretching surface, which ultimately lessens the concentration of nanoparticles in the boundary layer region.

Figure 18. Delineation of $\phi(\xi)$ for various λ.

Figure 19. Delineation of $\phi(\xi)$ for various N.

Figure 20. Delineation of $\phi(\xi)$ for various N_t.

Figure 21. Delineation of $\phi(\xi)$ for various N_b.

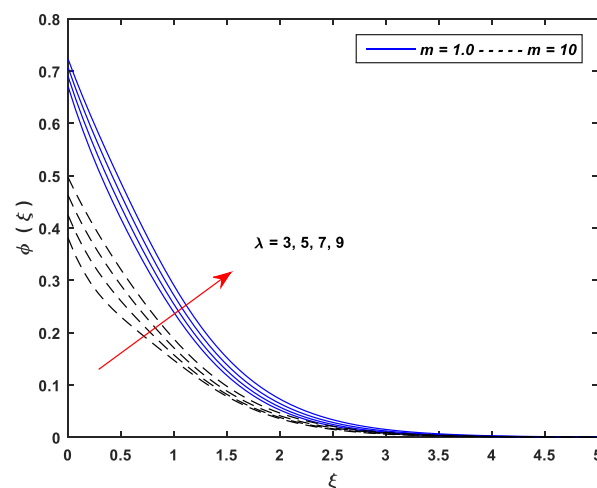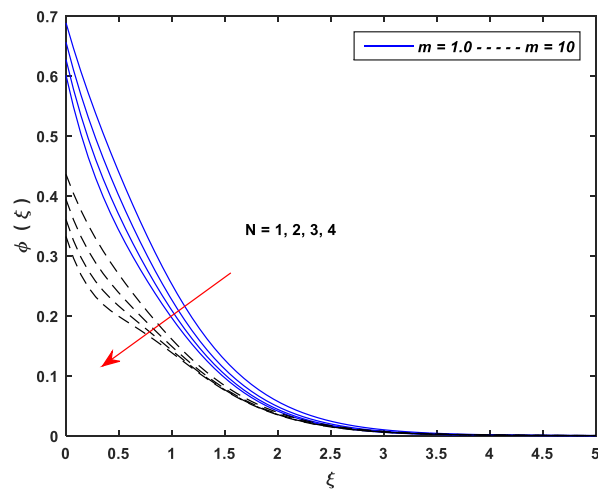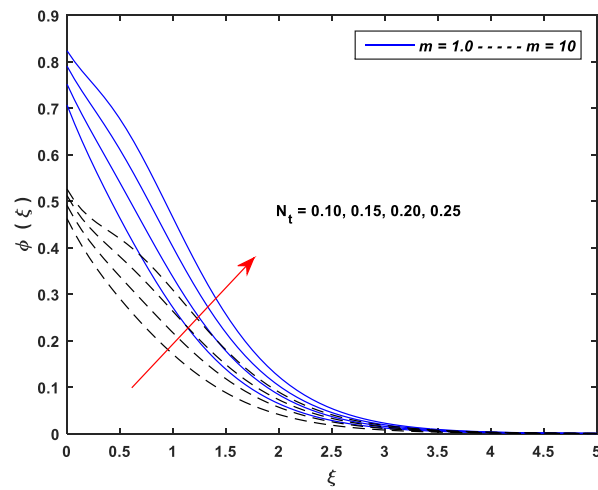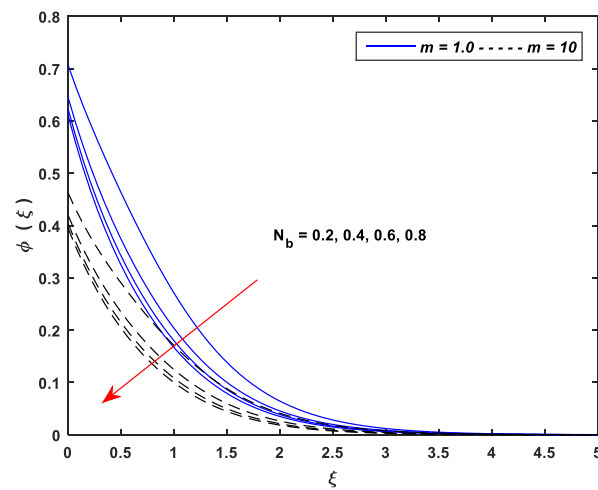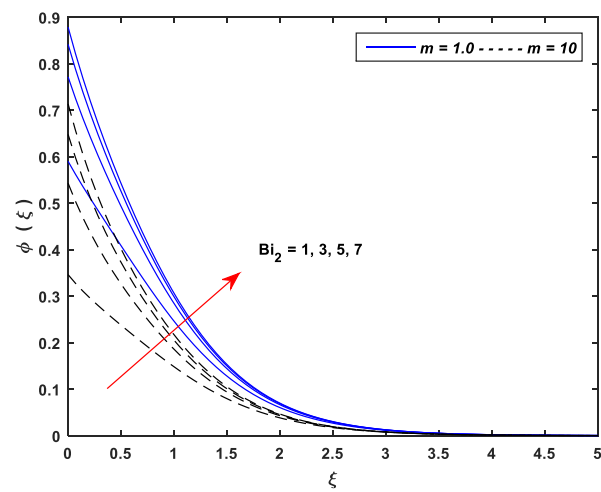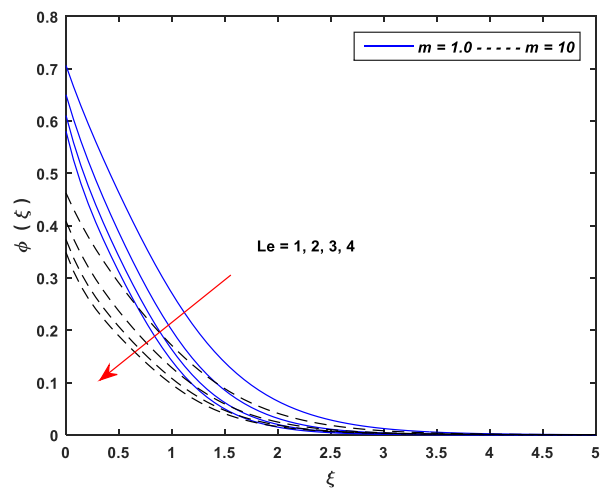**Figure 22.** Delineation of $\phi(\xi)$ for various Bi_2.

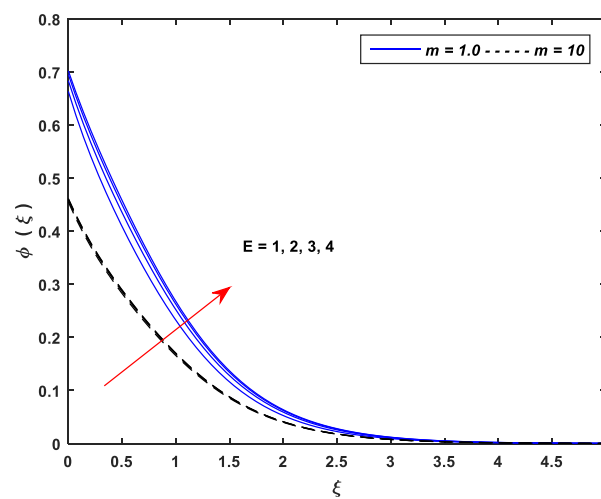**Figure 23.** Delineation of $\phi(\xi)$ for various Le.

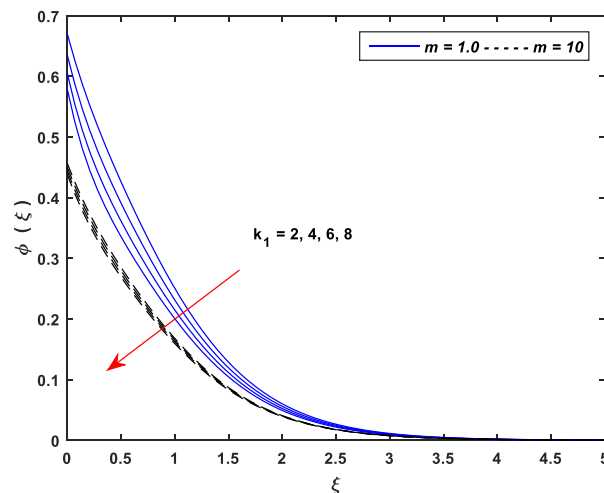**Figure 24.** Delineation of $\phi(\xi)$ for various E.

Figure 25. Delineation of $\phi(\xi)$ for various k_1.

Figure 22 displays an escalating trend of concentration profiles with the improving values of solutal Biot number Bi_2. The larger solutal Biot number will enhance mass transfer rate and, hence, the concentration of nanoparticles. A decreasing trend of concentration profiles under enhancing Lewis number is mapped in Figure 23. Physically, diffusivity is inversely linked with the Lewis number. Enlargement of Le reduces the concentration of nanoparticles. Activation energy E and chemical reaction parameter k_1 show a contrasting effect on the concentration distribution of nanoparticles (see Figures 24 and 25), since the activation energy is the least possible extent of energy required to start a chemical reaction. Therefore, Arrhenius equation of chemical reaction states the fact that the higher the extent of activation energy, the greater the concentration of mass. Contrarily, the chemical reaction parameter diminishes the concentration profiles.

5.4. Entropy Generation Profiles

Figures 26–33 explore the impact of various parameters on the entropy generation number N_G. It is worth noting that the entropy generation number against nonlinear stretching (i.e., $m = 10$) is leading as compared to the linear stretching (i.e., $m = 1.0$) for all pertinent parameters of the flow regime. Physically, the nonlinear stretching surface abandons a huge amount of disorder in the flow regime causing a higher rate of irreversibility in the thermodynamic working system. Graphical data show that the entropy generation number is an incremental function of the parameters Br, Bi_1, Bi_2, Rd, N_t and N_b while a declining function of parameters β and Pr. Nevertheless, the behavior of Brownian motion and thermophoretic diffusion parameters in the vicinity of the surface of the sheet minimizes the entropy. The same is the case for the Prandtl number with an opposite trend. These behaviors of entropy generation number predominantly depend on the momentum, temperature and concentration gradients that signify the heat transfer and fluid friction irreversibilities in the flow region.
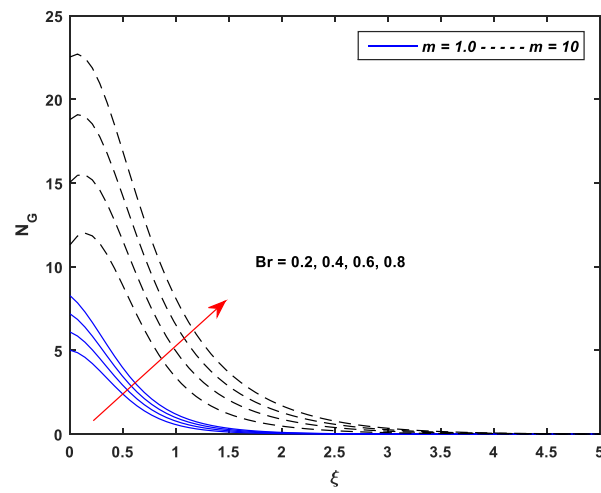
Figure 26. Delineation of $N_G(\xi)$ for various Br.
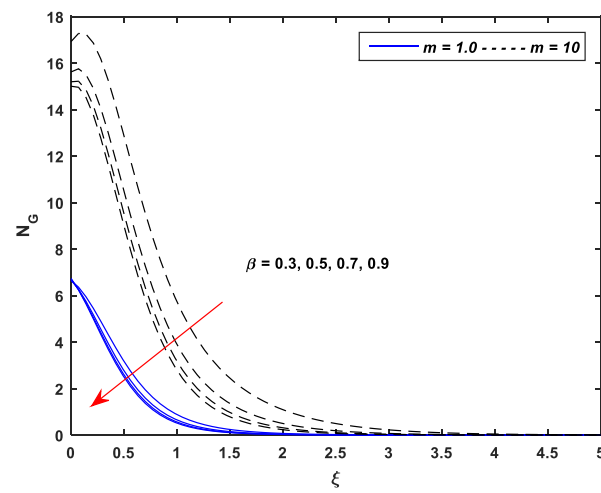
Figure 27. Delineation of $N_G(\xi)$ for various β.
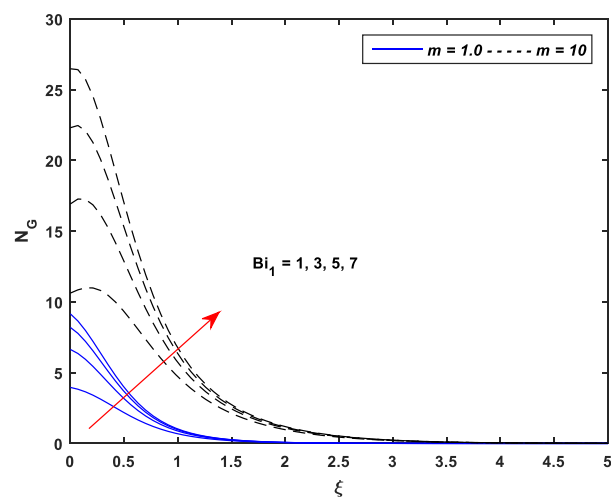
Figure 28. Delineation of $N_G(\xi)$ for various Bi_1.
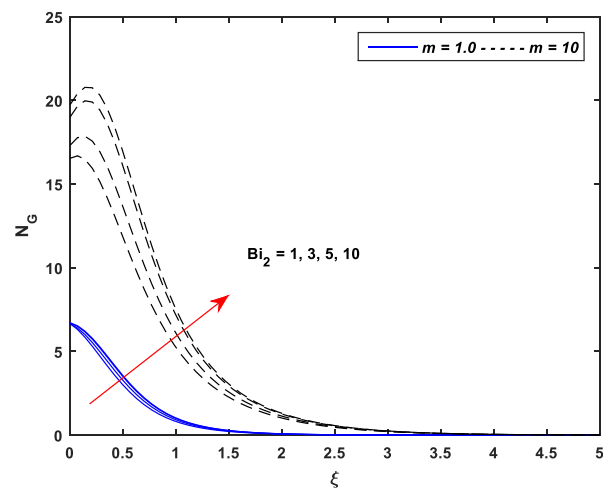
Figure 29. Delineation of $N_G(\xi)$ for various Bi_2.
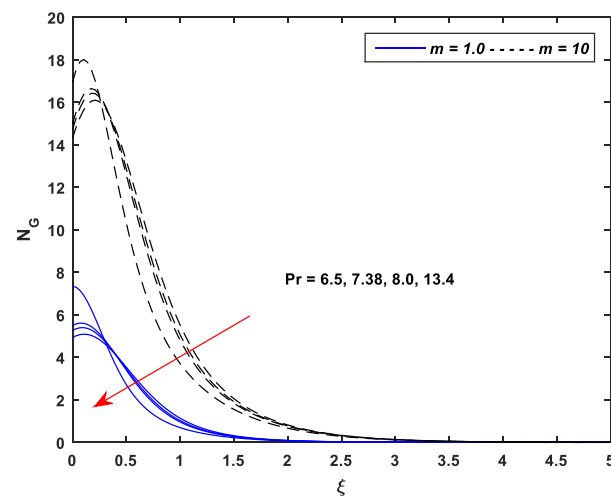
Figure 30. Delineation of $N_G(\xi)$ for various Pr.
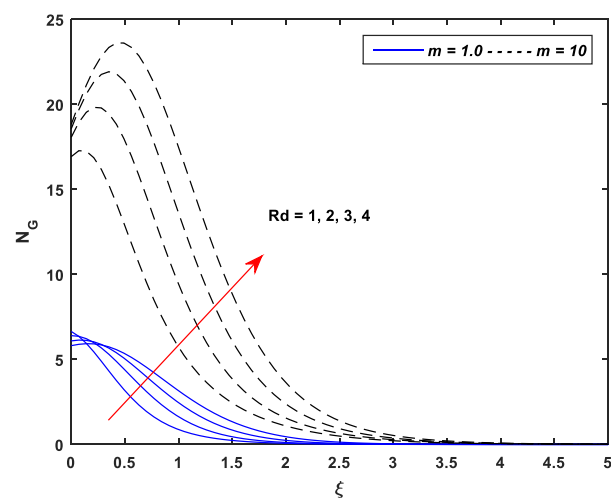
Figure 31. Delineation of $N_G(\xi)$ for various Rd.
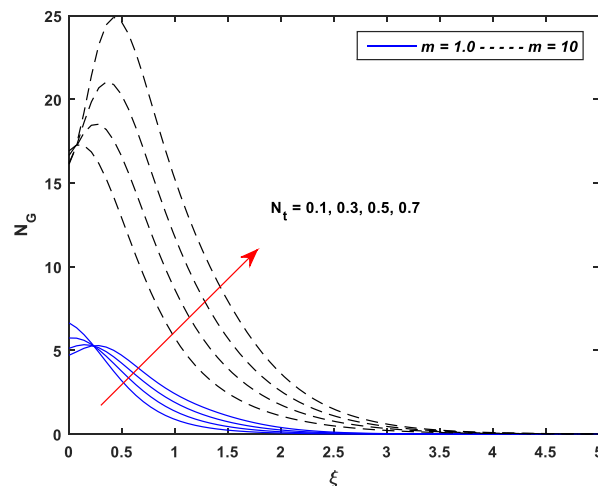
Figure 32. Delineation of $N_G(\xi)$ for various N_t.
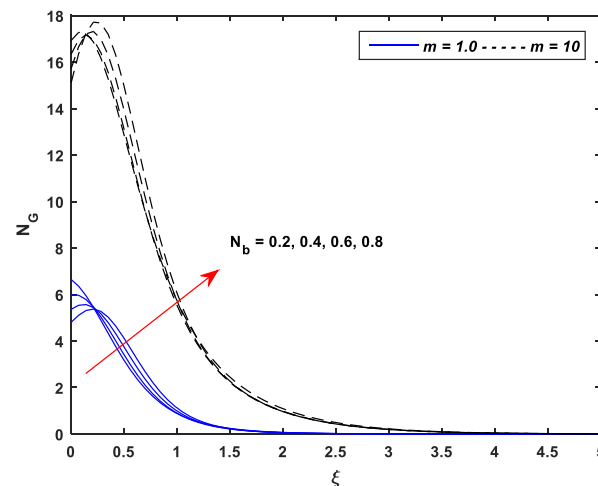
Figure 33. Delineation of $N_G(\xi)$ for various N_b.

6. Physical Quantities of Engineering Interest

The influence of different values of flow parameters on the numerical estimates of the skin friction coefficient ($Cf_x\mathrm{Re}_x^{\frac{1}{2}}$), Nusselt number ($Nu_x\mathrm{Re}_x^{\frac{-1}{2}}$) and Sherwood number ($Sh_x\mathrm{Re}_x^{\frac{-1}{2}}$) is explicated in Tables 1 and 2. A novel numerical contrast of linear and nonlinear stretching in the sheet is tabulated for physical quantities of engineering applications against several pertinent dimensionless parameters. It is observed that the magnitude of skin friction coefficient enhances for increasing values of Rd, β, Ec, δ, Bi_1, Bi_2, λ, ε, N_t, N, k_1 and E while it is a lessening function of Pr, M, Le, and N_b. However, the magnitude of skin friction in the case of nonlinear stretching dominates the linear stretching for all aforementioned parameters. The heat transference rate grows with the enhancing values of parameters Pr, Rd, β, δ, Le, k_1 and Bi_1, whereas a declining function in parameters M, Ec, Bi_2, λ, ε, N_t, N_b, E and N. Sherwood number that is representative of mass transference rate rises with enlarging the values of parameters M, Rd, Ec, Bi_2, Le, λ, ε, N_b, k_1 and N. However, a diminishing trend in mass transfer is noted against parameters Pr, β, δ, Bi_1, N_t and E.

Table 1. Numerical values of skin friction coefficient C_{fx}, Nusselt number Nu_x and Sherwood number Sh_x for fixed values of $Le = 1$, $\lambda = 5$, $N = 0.5$, $\varepsilon = 0.5$, $N_t = 0.1$, $N_b = 0.2$, $k_1 = 0.5$ and $E = 5$.

Pr	M	Rd	β	Ec	δ	Bi_1	Bi_2	Linear Stretching (m = 1.0)			Nonlinear Stretching (m = 10)		
								$Cf_x\mathrm{Re}_x^{\frac{1}{2}}$	$Nu_x\mathrm{Re}_x^{\frac{-1}{2}}$	$Sh_x\mathrm{Re}_x^{\frac{-1}{2}}$	$Cf_x\mathrm{Re}_x^{\frac{1}{2}}$	$Nu_x\mathrm{Re}_x^{\frac{-1}{2}}$	$Sh_x\mathrm{Re}_x^{\frac{-1}{2}}$
7.38	5	1	0.3	0.1	0.5	3	2	−2.0569	2.0705	0.5880	−3.9580	6.6033	2.5225
6.50								−2.0127	2.0215	0.6359	−3.4058	6.3840	2.6385
7.38								−2.0569	2.0705	0.5880	−3.9580	6.6033	2.5225
8.00								−2.2307	2.6936	0.3959	−4.6823	7.9332	2.3796
	2							−1.2522	2.3938	0.5796	−4.1249	8.6631	2.3350
	3							−1.5627	2.2560	0.5846	−4.0620	7.9686	2.3984
	5							−2.0569	2.0705	0.5880	−3.9580	6.6033	2.5225
		1						−2.0569	2.0705	0.5880	−3.9580	6.6033	2.5225
		2						−1.8494	2.4286	0.6672	−3.0301	8.2835	2.6653
		3						−1.6812	2.6148	0.7170	−2.2438	9.3106	2.7633
			0.3					−2.0569	2.0705	0.5880	−3.9580	6.6033	2.5225
			0.4					−1.7368	2.1591	0.5699	−3.3178	6.9686	2.4786
			0.5					−1.5323	2.2149	0.5582	−2.9036	7.2003	2.4498
				0.1				−2.0569	2.0705	0.5880	−3.9580	6.6033	2.5225
				0.2				−1.9087	1.5545	0.6638	−2.1724	3.1598	2.8806
				0.3				−1.7386	0.9730	0.7487	0.4449	−2.3094	3.4186
					1			−1.4760	2.2093	0.5532	−2.6048	6.9133	2.4712
					2			−0.9426	2.3126	0.5238	−1.5491	7.1415	2.4314
					3			−0.6922	2.3526	0.5110	−1.1027	7.2341	2.4147
						2		−2.1431	1.7297	0.6219	−4.3114	5.0947	2.6169
						4		−1.9997	2.2955	0.5658	−3.6926	7.7490	2.4516
						6		−1.9288	2.5737	0.5388	−3.3207	9.3719	2.3522
							1	−2.1399	2.1294	0.4108	−4.3904	6.8786	1.5333
							3	−2.0109	2.0375	0.6871	−3.6629	6.4114	3.2167
							5	−1.9613	2.0017	0.7946	−3.2843	6.1605	4.1298

Table 2. Numerical values of skin friction coefficient C_{fx}, Nusselt number Nu_x and Sherwood number Sh_x for fixed values of $\mathrm{Pr} = 6450$, $\beta = 0.3$, $\delta = 0.5$, $M = 5$, $Bi_1 = 3$, $Bi_2 = 2$, $Rd = 1$ and $Ec = 0.1$.

Le	λ	ε	N_t	N_b	N	k_1	E	Linear Stretching (m = 1.0)			Nonlinear Stretching (m = 10)		
								$Cf_x\mathrm{Re}_x^{\frac{1}{2}}$	$Nu_x\mathrm{Re}_x^{-\frac{1}{2}}$	$Sh_x\mathrm{Re}_x^{-\frac{1}{2}}$	$Cf_x\mathrm{Re}_x^{\frac{1}{2}}$	$Nu_x\mathrm{Re}_x^{-\frac{1}{2}}$	$Sh_x\mathrm{Re}_x^{-\frac{1}{2}}$
1	5	0.5	0.1	0.2	0.5	0.5	5	−2.0569	2.0705	0.5880	−3.9580	6.6033	2.5225
3								−2.2710	2.1076	0.8862	−4.9178	7.1047	3.1427
5								−2.3261	2.1325	1.0030	−5.1124	7.2187	3.3437
	3							−2.5725	2.1562	0.5556	−6.3210	7.5287	2.3616
	5							−2.0569	2.0705	0.5880	−3.9580	6.6033	2.5225
	7							−1.5259	1.9566	0.6226	−1.2865	5.4147	2.7014
		0.1						−2.1670	2.5039	0.5244	−4.7874	8.3329	2.3381
		0.3						−2.0569	2.0705	0.5880	−3.9580	6.6033	2.5225
		0.7						−1.8019	1.1148	0.7273	−1.9781	2.2189	2.9742
			0.1					−2.0569	2.0705	0.5880	−3.9580	6.6033	2.5225
			0.2					−1.8532	1.9129	0.4212	−3.0659	5.9165	2.2900
			0.3					−1.6681	1.7556	0.3002	−2.2718	5.2373	2.1905
				0.2				−1.9023	2.1395	0.3580	−3.2647	6.4004	2.1942
				0.4				−2.0569	2.0705	0.5880	−3.9580	6.5409	2.5225

Table 2. *Cont.*

Le	λ	ε	N_t	N_b	N	k_1	E	Linear Stretching ($m = 1.0$)			Nonlinear Stretching ($m = 10$)		
								$Cf_x\mathrm{Re}_x^{\frac{1}{2}}$	$Nu_x\mathrm{Re}_x^{-\frac{1}{2}}$	$Sh_x\mathrm{Re}_x^{-\frac{1}{2}}$	$Cf_x\mathrm{Re}_x^{\frac{1}{2}}$	$Nu_x\mathrm{Re}_x^{-\frac{1}{2}}$	$Sh_x\mathrm{Re}_x^{-\frac{1}{2}}$
				0.6				−2.0902	1.9707	0.6694	−4.1510	6.6033	2.6524
					1			−1.5483	1.9574	0.6233	−2.1734	5.7906	2.6467
					2			−0.6506	1.6999	0.6878	0.6823	4.3577	2.8435
					3			0.1247	1.4286	0.7456	2.9520	3.1026	3.0005
						2		−2.0762	2.0765	0.6203	−3.9735	6.6115	2.5343
						4		−2.1000	2.0837	0.6601	−3.9938	6.6327	2.5498
						6		−2.1217	2.0902	0.6966	−4.0136	6.6425	2.5650
							1	−2.1188	2.0818	0.6730	−4.0139	6.6320	2.5568
							3	−2.0714	2.0739	0.6094	−3.9700	6.6096	2.5306
							5	−2.0569	2.0693	0.5880	−3.9580	6.6033	2.5225

7. Conclusions

A novel numerical exploration of MHD Casson nanofluid over a nonlinear stretching sheet is presented in this study. The modelled partial differential equations are transmuted to a system of nonlinear differential equations with the help of similarity variables. The energy equation of the flow is improved with the heat generation, thermal radiation, viscous dissipation and joule heating terms. The numerical results obtained through an iterative procedure based on the quasi-linearization method (QLM) were deliberated against various dimensionless parameters. Brownian motion, thermophoretic diffusion and activation energy effects are also taken into account in the analysis. Impacts of various dimensionless parameters on velocity, temperature and concentration profiles are numerically estimated through graphs and tables. The main outcomes of the present study are listed below:

- Growing values of M, β and δ cause a significant decline in the velocity while N exhibits an opposite trend.
- Thermal profiles fall off with enhancing values of β and Pr, whereas increasing values of M, λ, Ec, R_d, N_t and N_b improve thermal profiles significantly.
- Improving the values of λ, N_t, Bi_2 and E upsurge the concentration profiles; however, the parameters N, N_b, Le and k_1 cause a remarkable reduction in the concentration distributions.
- The linear stretching dominates the nonlinear stretching for all controlling parameters of the concentration profiles.
- Entropy generation is an incremental function of the parameters Br, Bi_1, Bi_2, Rd, N_t and N_b while a declining function of parameters β and Pr.
- Implications of Brownian motion and thermophoresis are to minimize the entropy generation near the surface of the stretching sheet while maximizing the sheet.
- Entropy generation against nonlinear stretching leads as compared to the linear stretching for all pertinent parameters of the MHD flow of Casson nanofluid.
- Nusselt number and Sherwood number decrease significantly with growing values of activation energy in the case of nonlinear stretching.

The quasi-linearization method (QLM) could be applied to a variety of physical and technical challenges in the future [59–61].

Data Availability Statement: Data will be provided by the authors on request.

Conflicts of Interest: The authors announce no conflicts of interest.

Nomenclature

g	acceleration due to gravity (ms^{-2})	Re	Reynolds number
T_f	temperature of fluid (K)	Le	Lewis number
C_p	specific heat at constant pressure ($J\ mol^{-1}\ k^{-1}$)	Pr	Prandtl number
B_0	magnetic field strength ($kg\ s^{-2}\ A^{-1}$)	Ec	Eckert number
k	thermal conductivity ($W\ m^{-1}\ k^{-1}$)	Gr	Grashof number
D^*	molecular diffusivity ($m^2\ s^{-1}$)	Br	Brinkman number
C	fluid concentration ($mol\ m^{-3}$)		
Bi_1	thermal Biot number		
Bi_2	solutalBiot number	***Greek Symbols***	
q_r	radiative heat flux (Wm^{-2})	μ	fluid viscosity (kg $m^{-1}s^{-1}$)
M	magnetic parameter	ρ	fluid density (kg m^{-3})
Q	heat generation coefficient (W)	β	Casson parameter
E_a	activation energy factor ($J \cdot mol^{-1}$)	σ	electrical conductivity (Sm^{-1})
N_t	thermophoresis parameter	ψ	stream function ($m^2\ s^{-1}$)
N_b	Brownian motion parameter	θ	dimensionless temperature
k_r	rate of reaction (s^{-1})	λ	mixed convection parameter
m	index parameter	ϕ	dimensionless concentration
u, v	components of velocity (ms^{-1})	η	similarity variable
x, y	Cartesian coordinates along the stretching sheet, respectively (m)	γ	dimensionless reaction rate
		ε	heat generation parameter
		δ	slip parameter

References

1. Cui, X.; Wang, J.; Xia, G. Enhanced thermal conductivity of nanofluids by introducing Janus particles. *Nanoscale* **2022**, *14*, 99–107. [CrossRef] [PubMed]
2. Choi, S.U.; Eastman, J.A. *Enhancing Thermal Conductivity of Fluids with Nanoparticles*; No. ANL/MSD/CP-84938; CONF-951135-29; Argonne National Lab.: Argonne, IL, USA, 1995.
3. Choi, S.U. Nanofluid Technology: Current Status and Future Research; Illinois, University of North Texas Libraries, UNT Digital Library. 1998. Available online: https://digital.library.unt.edu (accessed on 12 September 2022).
4. Ahmad, S.; Akhter, S.; Shahid, M.I.; Ali, K.; Akhtar, M.; Ashraf, M. Novel thermal aspects of hybrid nanofluid flow comprising of manganese zinc ferrite MnZnFe$_2$O$_4$, nickel zinc ferrite NiZnFe$_2$O$_4$ and motile microorganisms. *Ain Shams Eng. J.* **2022**, *13*, 101668. [CrossRef]
5. Ali, K.; Faridi, A.A.; Ahmad, S.; Jamshed, W.; Khan, N.; Alam, M.M. Quasi-linearization analysis for heat and mass transfer of magnetically driven 3rd-grade (Cu-TiO$_2$/engine oil) nanofluid via a convectively heated surface. *Int. Commun. Heat Mass Transf.* **2022**, *135*, 106060. [CrossRef]
6. Ayub, R.; Ahmad, S.; Ahmad, S.; Akhtar, Y.; Alam, M.M.; Mahmoud, O. Numerical Assessment of Dipole Interaction with the Single-Phase Nanofluid Flow in an Enclosure: A Pseudo-Transient Approach. *Materials* **2022**, *15*, 2761. [CrossRef] [PubMed]
7. Li, J.; Zhang, X.; Xu, B.; Yuan, M. Nanofluid research and applications: A review. *Int. Commun. Heat Mass Transf.* **2021**, *127*, 105543. [CrossRef]
8. Asim, M.; Siddiqui, F.R. Hybrid Nanofluids Next Generation Fluids for Spray Cooling Based Thermal Management of High Heat Flux Devices. *Nanomaterials* **2022**, *12*, 507. [CrossRef]
9. Doan, D.Q. Interfacial characteristics and their impact on the indentation behavior of CuTa/CuTa amorphous/amorphous nanolaminates. *Int. J. Mech. Sci.* **2022**, *223*, 107297. [CrossRef]
10. Ekiciler, R.; Çetinkaya, M.S.A.; Arslan, K. Heat transfer enhancement in an equilateral triangular duct by using an Al$_2$O$_3$/water nanofluid: Effect of nanoparticle shape and volume fraction. *Heat Transf. Res.* **2020**, *51*, 741–757. [CrossRef]
11. Yadav, P.; Gupta, S.M.; Sharma, S.K. A review on stabilization of carbon nanotube nanofluid. *J. Therm. Anal. Calorim.* **2022**, *147*, 6537–6561. [CrossRef]

12. Arslan, K.; Ekiciler, R. Effects of SiO$_2$/Water Nanofluid Flow in a Square Cross-Sectioned Curved Duct. *Eur. J. Eng. Sci. Tech.* **2019**, *3*, 101–109.

13. Ahmad, S.; Ashraf, M.; Ali, K. Nanofluid flow comprising gyrotactic microorganisms through a porous medium. *J. Appl. Fluid Mech.* **2020**, *13*, 1539–1549.

14. Ahmad, S.; Ali, K.; Ashraf, M. MHD flow of Cu-Al$_2$O$_3$/water hybrid nanofluid through a porous media. *J. Porous Media* **2021**, *24*, 61–73. [CrossRef]

15. Casson, N. A flow equation for pigment-oil suspensions of the printing ink type. In *Rheology of Disperse Systems*; Pergamon Press: Oxford, UK, 1959; pp. 84–104.

16. Shahzad, F.; Jamshed, W.; Sathyanarayanan, S.U.D.; Aissa, A.; Madheshwaran, P.; Mourad, A. Thermal analysis on Darcy-Forchheimer swirling Casson hybrid nanofluid flow inside parallel plates in parabolic trough solar collector: An application to solar aircraft. *Int. J. Energy Res.* **2021**, *45*, 20812–20834. [CrossRef]

17. Krishna, M.V.; Ahammad, N.A.; Chamkha, A.J. Radiative MHD flow of Casson hybrid nanofluid over an infinite exponentially accelerated vertical porous surface. *Case Stud. Therm. Eng.* **2021**, *27*, 101229. [CrossRef]

18. Venkatesan, J.; Sankar, D.S.; Hemalatha, K.; Yatim, Y. Mathematical analysis of Casson fluid model for blood rheology in stenosed narrow arteries. *J. Appl. Math.* **2013**, *2013*, 583809. [CrossRef]

19. Obalalu, A.M. Chemical entropy generation and second-order slip condition on hydrodynamic Casson nanofluid flow embedded in a porous medium: A fast convergent method. *J. Egypt. Math. Soc.* **2020**, *30*, 6. [CrossRef]

20. Salahuddin, T.; Arshad, M.; Siddique, N.; Alqahtani, A.S.; Malik, M.Y. Thermophyical properties and internal energy change in Casson fluid flow along with activation energy. *Ain Shams Eng. J.* **2020**, *11*, 1355–1365. [CrossRef]

21. Hirpho, M. Mixed convection of Casson fluid in a differentially heated bottom wavy wall. *Heliyon* **2021**, *7*, e07361. [CrossRef]

22. Ennaouri, M.; Hachem, E.K. Modeling and study of the arterial blood flow loaded with nanoparticles under squeezing action in presence of a magnetic field. In Proceedings of the E3S Web of Conferences, Bandung, Indonesia, 11–12 October 2022; EDP Sciences: Ulis, France, 2022; Voulme 336, p. 00033. [CrossRef]

23. Jamil, D.F.; Uddin, S.; Kamardan, M.G.; Roslan, R. The effects of magnetic Casson blood flow in an inclined multi-stenosed artery by using Caputo-Fabrizio fractional derivatives. *J. Adv. Res. Fluid Mech. Therm. Sci.* **2021**, *82*, 28–38. [CrossRef]

24. Hussain, S.M.; Jamshed, W.; Kumar, V.; Kumar, V.; Nisar, K.S.; Eid, M.R.; Yahia, I.S. Computational analysis of thermal energy distribution of electromagnetic Casson nanofluid across stretched sheet: Shape factor effectiveness of solid-particles. *Energy Rep.* **2021**, *7*, 7460–7477. [CrossRef]

25. Alotaibi, H.; Althubiti, S.; Eid, M.R.; Mahny, K.L. Numerical treatment of MHD flow of Casson nanofluid via convectively heated non-linear extending surface with viscous dissipation and suction/injection effects. *Comput. Mater. Contin.* **2020**, *66*, 229–245. [CrossRef]

26. Shafiq, A.; Rasool, G.; Alotaibi, H.; Aljohani, H.M.; Wakif, A.; Khan, I.; Akram, S. Thermally enhanced Darcy-Forchheimer Casson-water/glycerine rotating nanofluid flow with uniform magnetic field. *Micromachines* **2021**, *12*, 605. [CrossRef] [PubMed]

27. Rasool, G.; Shafiq, A.; Khalique, C.M.; Zhang, T. Magnetohydrodynamic Darcy–Forchheimer nanofluid flow over a nonlinear stretching sheet. *Phys. Scr.* **2019**, *94*, 105221. [CrossRef]

28. Oyelakin, I.S.; Mondal, S.; Sibanda, P. Unsteady Casson nanofluid flow over a stretching sheet with thermal radiation, convective and slip boundary conditions. *Alex. Eng. J.* **2016**, *55*, 1025–1035. [CrossRef]

29. Matthew, O.L.; Kazeem, B.K.; Hammed, A.O.; Michael, O.O.; Yusuf, O.T.; Yussuff, T.L. On the mathematical model of Eyring–Powell nanofluid flow with non-linear radiation, variable thermal conductivity and viscosity. *Dyn. Partial. Differ. Equ.* **2022**, *5*, 100318.

30. Vishalakshi, A.B.; Mahabaleshwar, U.S.; Sarris, I.E. An MHD Fluid Flow over a Porous Stretching/Shrinking Sheet with Slips and Mass Transpiration. *Micromachines* **2022**, *13*, 116. [CrossRef] [PubMed]

31. Seid, E.; Haile, E.; Walelign, T. Multiple slip, Soret and Dufour effects in fluid flow near a vertical stretching sheet in the presence of magnetic nanoparticles. *Int. J. Therm. Fluids* **2022**, *13*, 100136. [CrossRef]

32. Alali, E.; Megahed, A.M. MHD dissipative Casson nanofluid liquid film flow due to an unsteady stretching sheet with radiation influence and slip velocity phenomenon. *Nanotechnol. Rev.* **2022**, *11*, 463–472. [CrossRef]

33. Sadiq, K.; Siddique, I.; Ali, R.; Jarad, F. Impact of Ramped Concentration and Temperature on MHD Casson Nanofluid Flow through a Vertical Channel. *J. Nanomater.* **2021**, *2021*, 3743876. [CrossRef]

34. Jawad, M.; Saeed, A.; Gul, T.; Bariq, A. MHD Darcy-Forchheimer flow of Casson nanofluid due to a rotating disk with thermal radiation and Arrhenius activation energy. *J. Phys. Commun.* **2021**, *5*, 025008. [CrossRef]

35. Yu, J.; Hu, F.; Zhu, Q.; Li, X.; Ren, H.; Fan, S.; Yang, D. PD-L1 monoclonal antibody-decorated nanoliposomes loaded with paclitaxel and P-gp transport inhibitor for the synergistic chemotherapy against multidrug resistant gastric cancers. *Nanoscale Res. Lett.* **2020**, *15*, 59. [CrossRef] [PubMed]

36. Al-Kouz, W.; Owhaib, W. Numerical analysis of Casson nanofluid three-dimensional flow over a rotating frame exposed to a prescribed heat flux with viscous heating. *Sci. Rep.* **2022**, *12*, 4256. [CrossRef] [PubMed]

37. Bejawada, S.G.; Reddy, Y.D.; Jamshed, W.; Nisar, K.S.; Alharbi, A.N.; Chouikh, R. Radiation effect on MHD Casson fluid flow over an inclined non-linear surface with chemical reaction in a Forchheimer porous medium. *Alex. Eng. J.* **2022**, *61*, 8207–8220. [CrossRef]

38. Bala Anki Reddy, P.; Jakeer, S.; Thameem Basha, H.; Reddisekhar Reddy, S.R.; Mahesh Kumar, T. Multi-layer artificial neural network modeling of entropy generation on MHD stagnation point flow of Cross-nanofluid. *Waves Random Complex Media* **2022**, 2067375. [CrossRef]

39. Kanti, P.; Sharma, K.V.; Minea, A.A.; Kesti, V. Experimental and computational determination of heat transfer, entropy generation and pressure drop under turbulent flow in a tube with fly ash-Cu hybrid nanofluid. *Int. J. Therm. Sci.* **2021**, *167*, 107016. [CrossRef]

40. Kanti, P.; Sharma, K.V.; Said, Z.; Kesti, V. Entropy generation and friction factor analysis of fly ash nanofluids flowing in a horizontal tube: Experimental and numerical study. *Int. J. Therm. Sci.* **2021**, *166*, 106972. [CrossRef]

41. Kanti, P.K.; Sharma, K.V.; Said, Z.; Gupta, M. Experimental investigation on thermo-hydraulic performance of water-based fly ash–Cu hybrid nanofluid flow in a pipe at various inlet fluid temperatures. *Int. Commun. Heat Mass Transf.* **2022**, *124*, 105238. [CrossRef]

42. Kanti, P.; Sharma, K.V.; Said, Z. Numerical study on the thermo-hydraulic performance analysis of fly ash nanofluid. *J. Therm. Anal. Calorim.* **2022**, *147*, 2101–2113. [CrossRef]

43. Ali, L.; Ali, B.; Ghori, M.B. Melting effect on Cattaneo–Christov and thermal radiation features for aligned MHD nanofluid flow comprising microorganisms to leading edge: FEM approach. *Comput. Math. Appl.* **2022**, *109*, 260–269. [CrossRef]

44. Kumar, M.D.; Raju, C.S.K.; Sajjan, K.; El-Zahar, E.R.; Shah, N.A. Linear and quadratic convection on 3D flow with transpiration and hybrid nanoparticles. *Int. Commun. Heat Mass Transf.* **2022**, *134*, 105995. [CrossRef]

45. Rasool, G.; Shafiq, A.; Khan, I.; Baleanu, D.; Sooppy Nisar, K.; Shahzadi, G. Entropy Generation and Consequences of MHD in Darcy–Forchheimer Nanofluid Flow Bounded by Non-Linearly Stretching Surface. *Symmetry* **2020**, *12*, 652. [CrossRef]

46. Rasool, G.; Shafiq, A.; Alqarni, M.S.; Wakif, A.; Khan, I.; Bhutta, M.S. Numerical Scrutinization of Darcy-Forchheimer Relation in Convective Magnetohydrodynamic Nanofluid Flow Bounded by Nonlinear Stretching Surface in the Perspective of Heat and Mass Transfer. *Micromachines* **2021**, *12*, 374. [CrossRef] [PubMed]

47. Rasool, G.; Saeed, A.M.; Lare, A.I.; Abderrahmane, A.; Guedri, K.; Vaidya, H. Darcy-Forchheimer Flow of Water Conveying Multi-Walled Carbon Nanoparticles through a Vertical Cleveland Z-Staggered Cavity Subject to Entropy Generation. *Micromachines* **2022**, *13*, 744. [CrossRef] [PubMed]

48. Shafiq, A.; Mebarek-Oudina, F.; Sindhu, T.N.; Rasool, G. Sensitivity analysis for Walters-B nanoliquid flow over a radiative Riga surface by RSM. *Sci. Iran.* **2022**, *29*, 1236–1249.

49. Batool, S.; Rasool, G.; Alshammari, N.; Khan, I.; Kaneez, H.; Hamadneh, N. Numerical analysis of heat and mass transfer in micropolar nanofluids flow through lid driven cavity: Finite volume approach. *Case Stud. Thermal Eng.* **2022**, *37*, 102233. [CrossRef]

50. Rasool, G.; Shafiq, A.; Hussain, S.; Zaydan, M.; Wakif, A.; Chamkha, A.J.; Bhutta, M.S. Significance of Rosseland's Radiative Process on Reactive Maxwell Nanofluid Flows over an Isothermally Heated Stretching Sheet in the Presence of Darcy-Forchheimer and Lorentz Forces: Towards a New Perspective on Buongiorno's Model. *Micromachines* **2022**, *13*, 368. [CrossRef]

51. Zari, I.; Shafiq, A.; Rasool, G.; Sindhu, T.N.; Khan, T.S. Double-stratified Marangoni boundary layer flow of Casson nanoliquid: Probable error application. *J. Thermal Anal. Calorim.* **2022**, *147*, 6913–6929. [CrossRef]

52. Sahoo, A.; Nandkeolyar, R. Entropy generation and dissipative heat transfer analysis of mixed convective hydromagnetic flow of a Casson nanofluid with thermal radiation and Hall current. *Sci. Rep.* **2021**, *11*, 3926. [CrossRef]

53. Sahoo, A.; Nandkeolyar, R. Entropy generation in convective radiative flow of a Casson nanofluid in non-Darcy porous medium with Hall current and activation energy. The multiple regression model. *Appl. Math. Comput.* **2021**, *402*, 125923. [CrossRef]

54. Ali, K.; Ahmad, S.; Nisar, K.S.; Faridi, A.A.; Ashraf, M. Simulation analysis of MHD hybrid CuAl$_2$O$_3$/H$_2$O nanofluid flow with heat generation through a porous media. *Int. J. Energy Res.* **2021**, *45*, 19165–19179. [CrossRef]

55. Ahmad, S.; Ali, K.; Nisar, K.S.; Faridi, A.A.; Khan, N.; Jamshed, W.; Khan, T.M.Y.; Saleel, A. Features of Cu and TiO$_2$ in the flow of engine oil subject to thermal jump conditions. *Sci. Rep.* **2021**, *11*, 19592. [CrossRef]

56. Ahmad, S.; Ali, K.; Faridi, A.A.; Ashraf, M. Novel thermal aspects of hybrid nanoparticles Cu-TiO$_2$ in the flow of ethylene glycol. *Int. Commun. Heat Mass Transf.* **2021**, *129*, 105708. [CrossRef]

57. Nisar, K.S.; Faridi, A.A.; Ahmad, S.; Khan, N.; Ali, K.; Jamshed, W.; Abdel-Aty, A.-H.; Yahia, I.S. Cumulative Impact of Micropolar Fluid and Porosity on MHD Channel Flow: A Numerical Study. *Coatings* **2022**, *12*, 93. [CrossRef]

58. Vajravelu, K. Viscous flow over a nonlinearly stretching sheet. *Appl. Math. Comput.* **2001**, *124*, 281–288. [CrossRef]

59. Jamshed, W.; Aziz, A. Entropy Analysis of TiO$_2$-Cu/EG Casson Hybrid Nanofluid via Cattaneo-Christov Heat Flux Model. *Appl. Nanosci.* **2018**, *8*, 1–14.

60. Jamshed, W. Numerical Investigation of MHD Impact on Maxwell Nanofluid. *Int. Commun. Heat Mass Transf.* **2021**, *120*, 104973. [CrossRef]

61. Jamshed, W.; Nisar, K.S. Computational single phase comparative study of Williamson nanofluid in parabolic trough solar collector via Keller box method. *Int. J. Energy Res.* **2021**, *45*, 10696–10718. [CrossRef]